



# 3D Nanostructured Nickel Hydroxide as an Efficient Electrocatalyst for Oxygen Evolution Reaction

Tong Li<sup>1</sup> · Xinxia Ma<sup>1</sup> · Daolei Wang<sup>1</sup> · Jiang Wu<sup>1</sup> · Fasong Zheng<sup>2</sup> · Jiawen Jin<sup>2</sup> · Qikun Wang<sup>2</sup> · Liangsheng Hao<sup>1</sup> · Zhaojie Li<sup>1</sup> · Sijia Huang<sup>1</sup>

Accepted: 20 June 2022 / Published online: 5 August 2022  
© The Author(s), under exclusive licence to Springer Science+Business Media, LLC, part of Springer Nature 2022

## Abstract

The exploration of high-efficiency and reliable non-precious metal electrocatalysts for overall water splitting is greatly vital and challenging for scientists to explore the physical structure effects with OER catalysts. Herein, we firstly developed three-dimensional alpha-nickel hydroxide as an advantageous electrocatalyst for OER by a simple solvothermal method. By controlling the solvent, two kinds of regular and one kind of irregular pure alpha-nickel hydroxide were successfully synthesized. Two regular catalysts' catalytic activity can be enhanced by the level of regularity increasing. Interestingly, with the increase of irregularity, compared with nanosphere-like Ni(OH)<sub>2</sub>, nanoparticle-sphere-like Ni(OH)<sub>2</sub> sample's specific surface areas, the number of ion transport channels, and reaction kinetics performance also raise, which actually enhances catalytic activity. In a word, the most irregular Ni(OH)<sub>2</sub>-NPS has the best electrocatalytic activity ( $\eta = 250$  mV) and the lowest Tafel slope (73.9 mV dec<sup>-1</sup>), and the outstanding constancy (8 h) at 1.48 V (vs. RHE) could be achieved, meanwhile, the benchmark RuO<sub>2</sub> (340 mV and 87.4 mV dec<sup>-1</sup>) is also inferior to Ni(OH)<sub>2</sub>-NPS. By comparing three Ni(OH)<sub>2</sub> samples, this work provides a new single transition metal system for about 3D materials and facilitates the development of highly efficient water oxidation catalysts.

**Keywords** 3D electrocatalyst materials · Single transition metal · Water oxidation

## Introduction

Facing the rapidly growing global economy and rising energy demands, major global groups have to face critical energy and environmental crises by developing clean and promising high cost-effective energy storage technologies [1–5]. Electrochemical oxidation of water (2H<sub>2</sub>O → 2H<sub>2</sub> + O<sub>2</sub>), which is the only truly plentiful and attractive candidate, can convert electrical energy and provide fuel cells with an environmental and sustainable to produce hydrogen (H<sub>2</sub>) and oxygen (O<sub>2</sub>) to achieve the storage of clean energy from renewable but unsustainable sources,

such as wind power, solar power, and tidal power [6–12]. Therefore, water splitting is a significant way of generating oxygen and hydrogen as clean and environmentally friendly fuel sources to solve the world energy crisis issue. Water splitting has two parts of reaction, in which oxygen evolution reaction (OER), 4OH<sup>-</sup> → O<sub>2</sub> + 2H<sub>2</sub>O + 4e<sup>-</sup>, is an enabling process for many energy storages and conversion options, such as water-splitting and rechargeable metal-air batteries [13–15]. However, OER requires a high overpotential to overcome the sluggish kinetics. An efficient and appropriate catalyst for OER is crucial to reduce the overpotential and kinetically accelerate the reaction of electrolytic water. Presently, many high-performance OER catalysts have been proposed, and most of them are precious-metal-based ruthenium (Ru) and iridium (Ir) oxides in acidic or alkaline solutions, which are the benchmark catalysts for OER but the scarcity and the low economic efficiency of precious metal severely hinder their applications widely [16, 17]. Thus, it is urgent to develop non-noble metal catalysts, including high activity and good stability for OER. Fortunately, many transition-metal-based especially abundant 3D metals (Fe,

✉ Daolei Wang  
1584718906@qq.com

✉ Jiang Wu  
wjcf2002@163.com

<sup>1</sup> College of Energy and Mechanical Engineering, Shanghai University of Electric Power, Shanghai 200090, China

<sup>2</sup> Guizhou Jinyuan Weining Energy Company, China Power Investment Corporation, Biji, Guizhou, China

Co, Ni, and Mn) [18–21] show great potential as alternative catalysts for OER and have been developed deeply.

Among many reported non-precious transition metal-based oxygen evolution reaction catalysts, Ni-containing have caught extra attention due to their excellent water oxidation potential and cost-efficient. As shown in many works, the general strategy for high OER catalyst materials has been achieved with, for instance, Ni-containing doped heteroatoms such as  $\text{Ni}_x\text{Co}_{3-x}\text{O}_4$ , [22] FeNi layer double hydroxides(LDH)/3D carbon network, [23] Ce-NiCo LDH/CNT [24], etc., as well as nonmetal, such as sulfide [25], phosphides [26], borides [27], nitrides [28], etc., Ni-containing hybridized conductive substrates such as carbon fiber paper [29], graphenes [30], carbon nanotube (CNT) [31], Ni foam [32], etc., Ni-containing polymetallic oxides (hydroxides) [33, 34], and Ni-containing perovskites [35]. The Fe–Ni system has the most potential as a candidate in alkaline electrolyte solutions among these nickel-based electrocatalysts, and actually lots of research on Fe–Ni-based catalysts have been reported, such as NiFe LDH/C dot [36], NiFe LDH/ $\text{Cu}_3\text{P}$  [37], and NiFe/ $\text{MoO}_4^{2-}$ , [38] have shown the most advanced OER performances (the overpotentials are 195–400 mV). It is worth noting that these excellent catalysts not only have two/three dimensional or porous structures but also have appropriate composition, single or multiple metal oxides, phosphides, nitrides, etc. Meanwhile,  $\text{Ni}(\text{OH})_2$ -based electrocatalysis has also received wide attention, Stern and Hu successfully synthesized  $\text{NiO}_x$  and  $\text{Ni}(\text{OH})_2$  nanoparticles and demonstrated that nanostructures play an important role in catalytic activity [39]. Agoston et al. prepared  $\text{Ni}(\text{OH})_2$  by electrodeposition and demonstrated the formation of NiO species after the OER reaction [40]. Lee et al. investigated the principle of OER reaction of  $\text{Ni}(\text{OH})_2$  on low- and high-density carbon paper and proposed a two-stage degradation mechanism for cyclic voltammetric (CV) cycling [41]. Kim et al. synthesized  $\beta$ - $\text{Ni}(\text{OH})_2$  nanoplates by hydrothermal method, revealing that the excellent OER properties and stability result from the abundant oxygen vacancies and well-defined hexagonal structure [42]. At present, through different combinations and a large number of experimental studies, the composition effect of the active site can be clearly clarified in most cases, these works could provide reasonable guidance for devising catalyst components in the future. The work of electrocatalyst design seems to have taken a single path. Compared with the composition effect, there are few studies about OER catalyst materials based on the effect of 3D structure, because the theoretical calculation cannot simulate the whole reaction process, such as diffusion and adsorption, but illustrate the electrochemical reaction from the atomic level and evolving different structures with invariant compositions is a huge experimental challenge. Therefore, we have only known that structures with a large surface and active sites, and so on are beneficial to the activity of

OER catalysts, while the understanding of structural effects is superficial and often relies on an accidental discovery.

Herein, we report that 3D nanostructured  $\text{Ni}(\text{OH})_2$  are stable, highly active, low overpotential catalysts for OER, which show better performance in alkaline electrolyte than ruthenium oxide ( $\text{RuO}_2$ ), and the synthetic process of 3D nanostructured  $\text{Ni}(\text{OH})_2$  is plain, environmentally friendly and easy to be popularized. Additionally, by comparing  $\text{Ni}(\text{OH})_2$ -nanoparticle ( $\text{Ni}(\text{OH})_2$ -NP),  $\text{Ni}(\text{OH})_2$ -nanosphere ( $\text{Ni}(\text{OH})_2$ -NS), and  $\text{Ni}(\text{OH})_2$ -nanoparticle-sphere ( $\text{Ni}(\text{OH})_2$ -NPS) through lots of professional morphological, spectroscopic, and electrochemical characterizations, the mechanism of the improvement of 3D  $\text{Ni}(\text{OH})_2$  electrocatalytic performance is revealed. This result strongly demonstrates the prospect of high-performance, credible, and cost-effective OER electrocatalysts based on  $\text{Ni}(\text{OH})_2$  Scheme 1 Illustration for synthesizing  $\alpha$ - $\text{Ni}(\text{OH})_2$  samples via the solvothermal method Scheme 1 Illustration for synthesizing  $\alpha$ - $\text{Ni}(\text{OH})_2$  samples via the solvothermal method

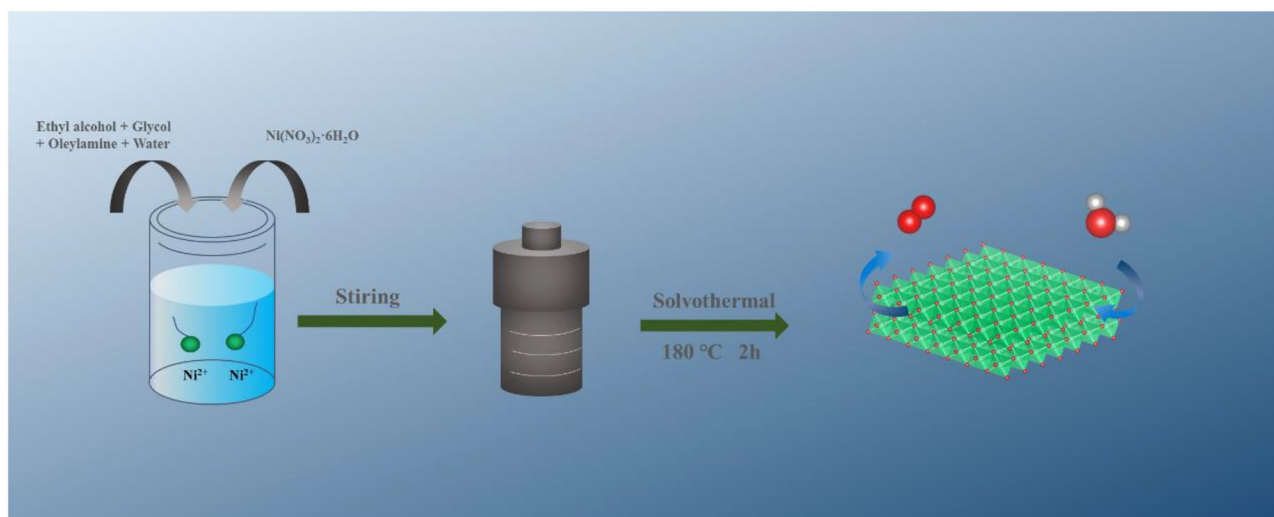
## Experimental Section

### Reagents and Chemicals

Nickel nitrate hexahydrate ( $\text{Ni}(\text{NO}_3)_2 \cdot 6\text{H}_2\text{O}$ ) (99%, GR), potassium hydroxide (KOH) (99.99%, GR), oleylamine (90%, GR), and ethylene glycol (99%, GR) were purchased from Adamas. Ethanol (95%, GR) and deionized water were purchased from Greagent. Nafion (5 wt%) and ruthenium (IV) oxide ( $\text{RuO}_2$ , 99.95%) were all purchased from Shanghai Titan Scientific Co., Ltd. All chemical reagents were analytically pure and were used as received without further purification.

### Synthesis of Three Nanostructure $\alpha$ - $\text{Ni}(\text{OH})_2$

A total of 0.582 g of  $\text{Ni}(\text{NO}_3)_2 \cdot 6\text{H}_2\text{O}$  was added into a mixed solution (40 mL of ethanol, 4 mL of oleylamine, 2 mL of deionized water, and 20 mL ethylene glycol), and kept stirring for about 30 min to produce a uniform green solution, and then transferred it into a 100-mL Teflon-lined autoclave and heated at 180 °C for 2 h. After the  $\text{Ni}(\text{OH})_2$ -NPS was cooled naturally, samples were washed with both deionized water and ethanol and dried at 80 °C for 12 h. For  $\text{Ni}(\text{OH})_2$ -NP, everything is the same except that 10 mL of deionized water was used. For  $\text{Ni}(\text{OH})_2$ -NS, everything is the same except without deionized water.



**Scheme 1** Illustration for synthesizing  $\alpha$ -Ni(OH)<sub>2</sub> samples via the solvothermal method

## Materials Characterization

The powder X-ray powder diffraction (XRD, Rigaku Ultima IV, Cu K $\alpha$  radiation,  $\lambda = 1.5418 \text{ \AA}$ ), and X-ray photoelectron spectroscopy (XPS, Thermo Scientific K-Alpha) were carried out to probe the composition of the samples. The scanning electron microscope (SEM, JSM-7800F), transmission electron microscopy (TEM, FEI G2 600–300), atomic force microscope (AFM, Bruker Dimension ICON), and N<sub>2</sub> adsorption/desorption isotherms (ASAP 2460 2.01,  $-195.8 \text{ }^\circ\text{C}$ ) were used to explore the structure of the samples.

## Electrocatalytic Study

A CHI760E electrochemical workstation (CHI Instruments, CHN) was applied to conduct electrochemical using a standard three-electrode system. A glassy carbon electrode (with 3 mm in diameter) was used as a working electrode, an Hg/HgO electrode with 1.0 M KOH filling solution was used as a reference electrode, and a graphite rod was used as a counter electrode throughout the experiment. A 0.1 M KOH solution was used as an electrolyte. The potentials measured in our work were referenced to the reversible hydrogen electrode (RHE) through the Nernst equation:

$$E(\text{RHE}) = E(\text{Hg}/\text{HgO}) + 0.865\text{V}$$

To produce the ink, we took 2 mg of catalyst powder and 1 mg carbon black into a 1.0 mL mixed solution (750  $\mu\text{L}$  of deionized water and 250  $\mu\text{L}$  of isopropyl alcohol), with 25  $\mu\text{L}$  of Nafion solution into the above solution at the same time. Then, the mixture was ultrasonicated for at least 0.5 h. To prepare RuO<sub>2</sub> ink, we also took 2 mg of RuO<sub>2</sub> catalyst

powder into a mixed solution (750  $\mu\text{L}$  of deionized water, 250  $\mu\text{L}$  of isopropyl alcohol, and 25  $\mu\text{L}$  of Nafion solution), and the solution was ultrasonicated for at least 0.5 h. Afterward, the homogeneous ink was coated on the surface of the working electrode ( $0.2 \text{ mg cm}^{-2}$ ). Then, the as-prepared catalyst film was dried at room temperature.

The 0.1 M KOH electrolyte was saturated with pure oxygen. The linear sweep voltammetry (LSV) curves were recorded in the potential range between 1.1 and 1.9 V vs. RHE with a sweep rate of  $5 \text{ mV s}^{-1}$  at room temperature. We have measured 30 cycles of CV to stabilize electrodes between 1.0 and 2.0 V vs. RHE with a scan rate of  $50 \text{ mV s}^{-1}$  before the OER test. Tafel slopes were calculated based on the LSV curves by plotting overpotential against log (current density). The electrochemical impedance spectroscopy (EIS) measurement was carried out at the open circuit potential with a frequency range from  $10^{-2}$  to  $10^5$  Hz and an amplitude of 0.01 V. Chronopotentiometry measurement was performed to evaluate the long-term stability. Other electrocatalyst samples were measured with electrochemical tests under similar conditions.

## Results and Discussion

We successfully synthesized phase-controllable  $\alpha$ -Ni(OH)<sub>2</sub> in a simple solvothermal system. The morphologies of the samples were investigated by scanning electron microscope (SEM). It can be seen that these pure phase  $\alpha$ -Ni(OH)<sub>2</sub> samples have nanosphere-like (Ni(OH)<sub>2</sub>-NS) (Fig. 1a), nanoparticle-like (Ni(OH)<sub>2</sub>-NP) (Fig. 1d), and nanoparticle-sphere-like (Ni(OH)<sub>2</sub>-NPS) (Fig. 1g) morphology, respectively. The microstructures of as-prepared

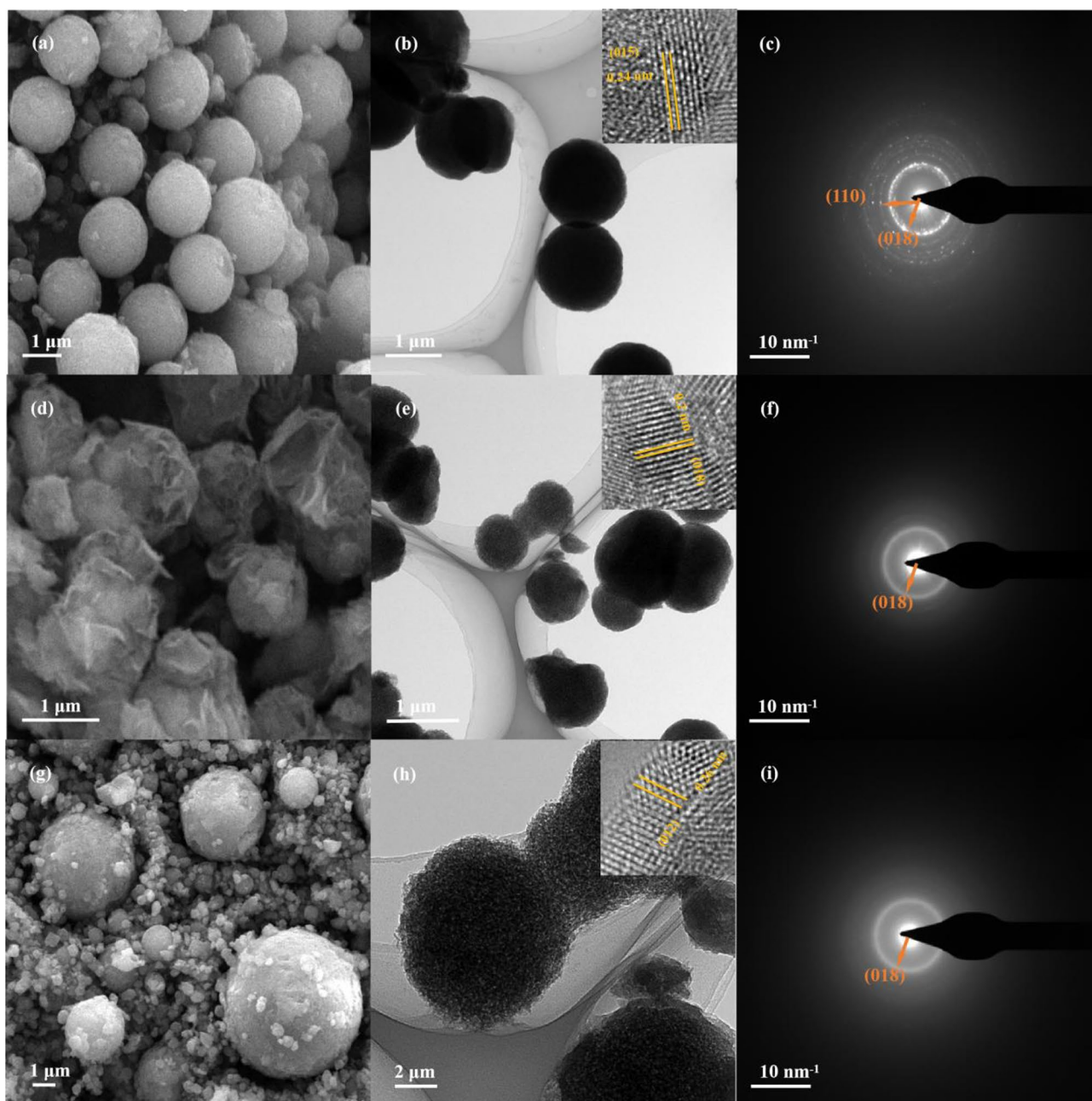


**Fig. 1** Representative **a** SEM, **b** TEM, and **c** SAED images of  $\text{Ni(OH)}_2\text{-NS}$ , representative; **d** SEM, **e** TEM, and **f** SAED images of  $\text{Ni(OH)}_2\text{-NP}$ , representative; **g** SEM, **h** TEM, and **i** SAED images

of  $\text{Ni(OH)}_2\text{-NPS}$ , representative. The upper right insets of (b), (e), and (h) are the HRTEM images of  $\text{Ni(OH)}_2\text{-NS}$ ,  $\text{Ni(OH)}_2\text{-NP}$ , and  $\text{Ni(OH)}_2\text{-NPS}$  with scale bars of 5 nm, respectively

phase-controllable samples were further carried out by transmission electron microscopy (TEM). TEM images show that the  $\text{Ni(OH)}_2\text{-NPS}$  (Fig. 1h) is constructed by countless ultrathin nanosheets. Selected-area electron diffraction (SAED) pattern extracted from a single nanoparticle/sphere shows that the nanosheets have polycrystalline properties due to their nanostructures (Fig. 1c, f, and i). In addition, the high-resolution TEM (HRTEM) was also used to reveal lattice fringes of  $\alpha\text{-Ni(OH)}_2$  (015), (018),

and (012) planes (inset Fig. 1b, e, and h), respectively. To compare the diverse structures of the above samples more persuasively, we also tested the most irregular sample ( $\text{Ni(OH)}_2\text{-NPS}$ ). The diameter of single  $\text{Ni(OH)}_2\text{-NPS}$  nanospheres was tested with a large variation, interestingly, both 4–5  $\mu\text{m}$  and 1–2  $\mu\text{m}$  exist, which was confirmed by TEM images. From the atomic force microscope (AFM) measurement (Supplementary Fig. S1), the thickness was 4.6 nm. What is more, it is clear to observe that

many nanoparticles (200–500 nm in diameter) cling to the large nanospheres, like stars around the planet, we define this phenomenon as the star effect. Noteworthy are the nanospheres and nanoparticles, which possess a more average diameter (average diameter 1–2  $\mu\text{m}$ ) and exhibit a better regularity.

X-ray diffraction (XRD) was firstly utilized to confirm the successful formation of pure  $\alpha\text{-Ni(OH)}_2$  (JCPDS 380,715) phases (Fig. 2a). The sharp characteristic peaks of three samples at  $2\theta = 10.5^\circ$  (003),  $21.2^\circ$  (006),  $34.1^\circ$  (101), and  $60.7^\circ$  (110) strongly prove the high purity of the three samples. Notably, the diffraction angles at  $2\theta = 10.5^\circ$  (003) and  $2\theta = 21.2^\circ$  (006) shift to lower angles compared with the blank  $\alpha\text{-Ni(OH)}_2$ , indicating the increase of distance along the  $c$ -axis stabilized by mutual calibration impurity ions intercalation. The asymmetrical reflection at  $2\theta = 34.1^\circ$  was indicated to form pure  $\alpha\text{-Ni(OH)}_2$ , which was reported in other  $\alpha\text{-Ni(OH)}_2$  electrocatalyst materials [43]. In addition, crystallographic analysis indicates that the average crystallite sizes are 1 nm along the  $c$ -axis, which agrees well with the spacing of the (003) reflection of  $\alpha\text{-Ni(OH)}_2$ , demonstrating that per crystallite of the hydroxides has one sheet (Table S1). According to Table S1, three typical  $\alpha\text{-Ni(OH)}_2$  samples were synthesized by a similar simple hydrothermal method, thus the thicknesses are similar, which is of great significance for studying the effect of structure on the properties of over with a single variable.

Next, we used X-ray photoelectron spectroscopy (XPS) to analyze the surface composition and electronic state of samples synthesized by the solvothermal method. Based on the XPS measurements spectrum of  $\alpha\text{-Ni(OH)}_2$  surface, the characteristic peaks of Ni and O can be clearly seen (Fig. 2b), and these are the same results as the XRD spectrum. High-resolution spectra of Ni 2p and O 1s were also presented in Fig. 2c and d, respectively. As shown in Ni 2p (Fig. 2c), the peak located at 855.5 eV was assigned to  $2P_{3/2}$  of the Ni–OH bonds and the binding energy peak at 873.1 eV belongs to  $2P_{1/2}$  of the Ni–OH bonds, meanwhile two satellite peaks were located at 861.1 eV and 879.2 eV. As for the O 1s spectrum (Fig. 2d), the binding energy at 531.08 and 532.78 eV suggest the existence of  $\text{O}^{2-}$  in  $\alpha\text{-Ni(OH)}_2$ , indicating characteristic peaks of the Ni–O bonds and absorbed water, respectively. The electronic states of Ni and O were the best coincidence with the simulation model of nickel hydroxide molecules.

To probe the specific surface area and the surface physical properties, nitrogen adsorption–desorption isotherms were applied. Just as Fig. 2e shows, the results indicate that all the synthesized  $\alpha\text{-Ni(OH)}_2$  samples own IV type isotherms and H3-type hysteresis loops, and the mesoporous sizes of three samples are narrow (Fig. 2f).  $\text{Ni(OH)}_2\text{-NPS}$  exhibits a large (Brunauer–Emmett–Teller) BET-specific surface area of  $132.7 \text{ m}^2\text{g}^{-1}$ , while the BET-specific

surface areas of  $\text{Ni(OH)}_2\text{-NS}$  is only  $89.1 \text{ m}^2\text{g}^{-1}$  and that of  $\text{Ni(OH)}_2\text{-NP}$  is  $122.9 \text{ m}^2\text{g}^{-1}$ . Boiled reaction solutions (i.e., ethanol, ethylene glycol, oleylamine, and deionized water) can generate stable emulsions and bubbles under a solvent heat environment at  $180^\circ\text{C}$ . The newly formed tiny  $\alpha\text{-Ni(OH)}_2$  crystals attach to the gas–liquid interface, grow along with the generated bubbles, and finally form a nanosphere. Due to the addition of deionized water, the size and density of the bubbles generated during the boiling of the reaction solution vary.  $\text{Ni(OH)}_2\text{-NS}$  without the addition of deionized water grows nanospheres with better morphology but smaller diameter depending on the abundant fine bubbles.  $\text{Ni(OH)}_2\text{-NPS}$  with the addition of moderate amounts of deionized water, the fine bubbles are more likely to aggregate into larger bubbles and finally form some nanospheres with a larger diameter, as well as nanoparticles. Adding a large amount of deionized water of  $\text{Ni(OH)}_2\text{-NP}$ , it is difficult to form more complete nanospheres with the addition of more deionized water, and finally, presents the appearance of nanoparticles. The spherical shape has the largest specific surface area for the same mass, therefore, nanoparticle spheres with larger diameters have the largest specific surface area. However, nanoparticles own a larger specific surface area than that of nanospheres, although both of them have similar diameters, and this fact may indicate that nanoparticle plays an important role in the specific surface area. Actually, classical fracture pores formed by the approximate average physical size of the similar pores size distribution are similar, and  $\text{Ni(OH)}_2\text{-NPS}$  owns a pore diameter of 6.7 nm, which is 0.88 and 1.48 times compared with that of  $\text{Ni(OH)}_2\text{-NS}$  and  $\text{Ni(OH)}_2\text{-NP}$ , respectively. In general, these significantly irregular  $\alpha\text{-Ni(OH)}_2$  samples have similar physical characteristics, providing a perfect univariate condition for studying the relationship between structure (irregularity in diameter and morphology) and OER performance.

The electrocatalytic capabilities of three  $\text{Ni(OH)}_2$  samples and benchmark metal  $\text{RuO}_2$  toward OER in electrolyte with 0.1 M KOH were measured, and before electrocatalytic tests, 10 cycles of CV tests were used to stabilize electrocatalysts' electrochemical performances. The obtained linear sweep voltammetry (LSV) curves are shown in Fig. 3a, illustrating  $\text{Ni(OH)}_2\text{-NPS}$  is the best catalyst among three samples synthesized by a simple hydrothermal method, because  $\text{Ni(OH)}_2\text{-NPS}$  only requires a small overpotential of 250 mV at  $j = 10 \text{ mA cm}^{-2}$  (Fig. 3d), while the overpotentials ( $j = 10 \text{ mA cm}^{-2}$ ) are 450, 500, and 340 mV for  $\text{Ni(OH)}_2\text{-NS}$ ,  $\text{Ni(OH)}_2\text{-NP}$ , and  $\text{RuO}_2$ , respectively. To reach  $\eta = 250 \text{ mV}$ , the current densities of  $\text{Ni(OH)}_2\text{-NPS}$  is  $10 \text{ mA cm}^{-2}$  (Fig. 3e).  $\text{Ni(OH)}_2\text{-NS}$  ( $1.66 \text{ mA cm}^{-2}$ ) and  $\text{Ni(OH)}_2\text{-NP}$  ( $1.11 \text{ mA cm}^{-2}$ ) have similar current density, both of them are lower than the current density of  $\text{RuO}_2$  ( $4.32 \text{ mA cm}^{-2}$ ). The above results illustrate that

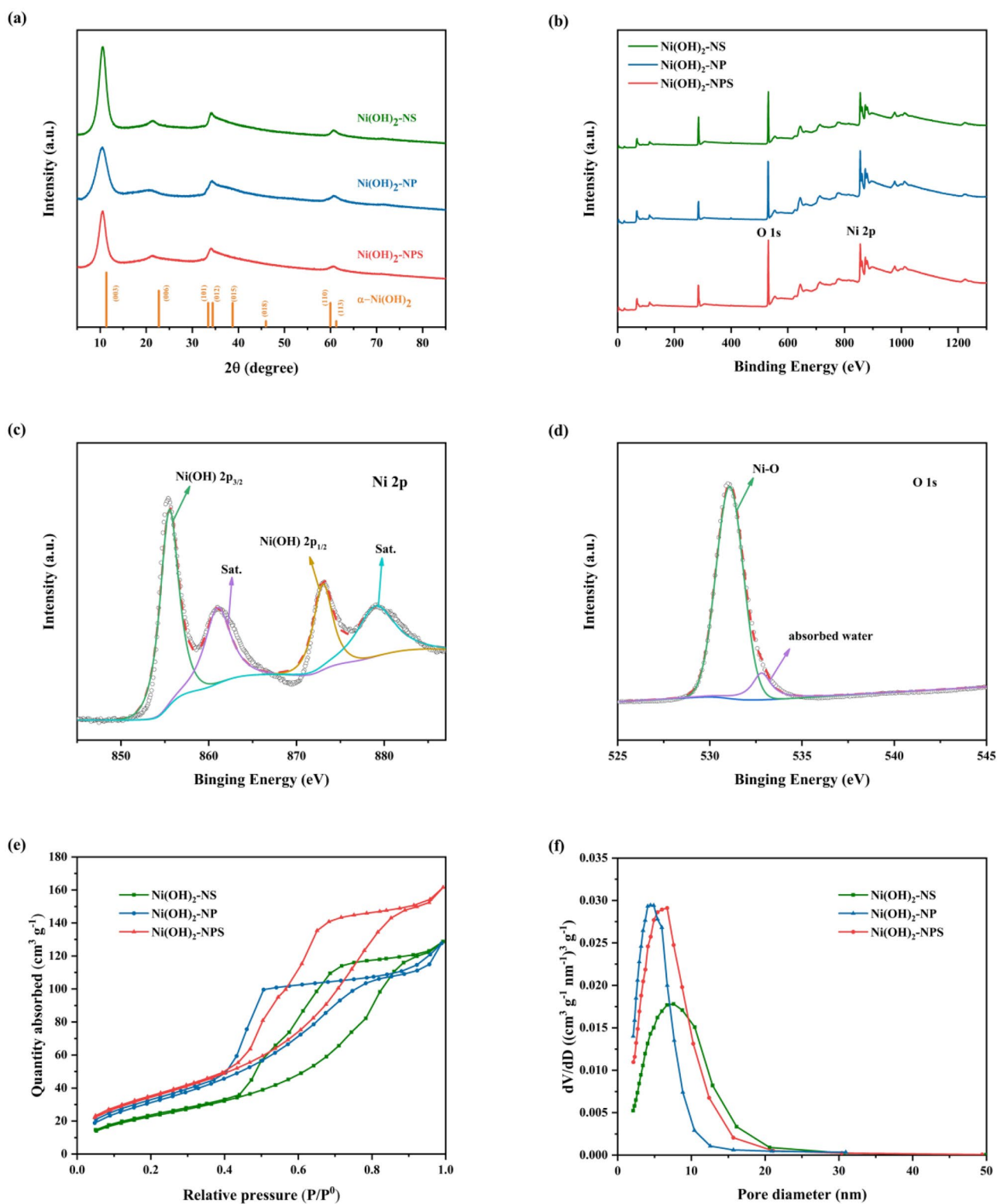


**Fig. 2** a X-ray diffraction (XRD) patterns of the three samples. The lines correspond to standard XRD patterns of  $\alpha$ -Ni(OH)<sub>2</sub> (JCPDS 380,715); b X-ray photoelectron spectroscopy (XPS) of three sam-

ples; high-resolution XPS spectra of Ni 2p (c), and O 1s (d); e N<sub>2</sub> adsorption/desorption isotherms and f pore-size distributions for the as-synthesized  $\alpha$ -Ni(OH)<sub>2</sub> samples

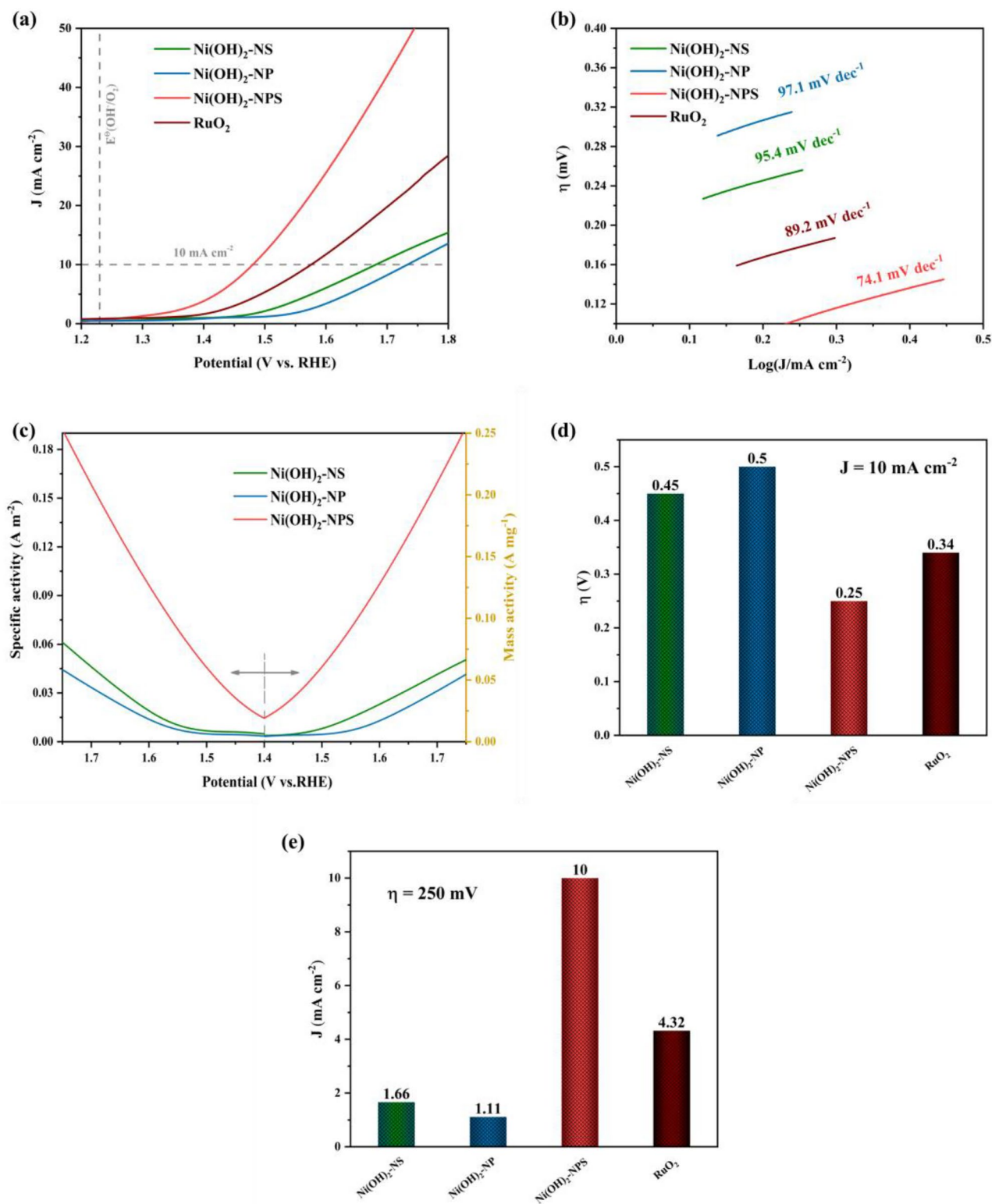


**Fig. 3** **a** LSV curves and **b** Tafel slopes of Ni(OH)<sub>2</sub>-NS, Ni(OH)<sub>2</sub>-NP, Ni(OH)<sub>2</sub>-NPS, and the benchmark RuO<sub>2</sub> catalyst; **c** mass activity and specific activity for the as-prepared  $\alpha$ -Ni(OH)<sub>2</sub> samples; **d** Overpotential at  $j = 10 \text{ mA cm}^{-2}$  and **e** Current density at  $\eta = 250 \text{ mV}$ . All measurements were performed in O<sub>2</sub>-purged 0.1 M KOH (pH ~ 13) with a

glass carbon electrode (GC). The catalyst loading was  $\sim 0.2 \text{ mg cm}^{-2}$ . The current density ( $j_{\text{geo}}$ ), specific activity ( $j_{\text{BET}}$ ), and mass activity ( $j_{\text{mass}}$ ) were normalized to their electrode geometric area, BET surface area, and the mass loading, respectively. All LSV curves were recorded at a sweep rate of  $5 \text{ mV s}^{-1}$ . LSV curves were iR corrected

Ni(OH)<sub>2</sub>-NPS just requires an assuredly low work voltage (1.48 V vs. RHE) to overcome the reaction energy barrier. Briefly, the nanoparticle-sphere structure may enhance OER performance.

For further assessing these samples, we distilled the kinetic parameters of the four catalysts from the Tafel slopes. Two regular samples deliver the similar Tafel slopes, and Ni(OH)<sub>2</sub>-NS (95.4 mV dec<sup>-1</sup>) and Ni(OH)<sub>2</sub>-NP (97.1 mV dec<sup>-1</sup>) are both larger than that of RuO<sub>2</sub> (89.2 mV dec<sup>-1</sup>). However Ni(OH)<sub>2</sub>-NPS has a Tafel slope of about only 74.1 mV dec<sup>-1</sup>, showing that Ni(OH)<sub>2</sub>-NPS has favorable kinetics of electrochemical oxygen evolution reaction. According to Tatsuya Shinagawa's report, when the surface adsorbed species produced in the early stage of the OER remains predominant, the Tafel slope decreases as it is lower than 120 mV dec<sup>-1</sup>. [44] In this work, the unexpectedly low Tafel slope of 74.1 mV dec<sup>-1</sup> was obtained for the Ni(OH)<sub>2</sub>-NPS a value that is obviously lower than other samples, indicating the ions transmission gets easier and easier as the shape irregularity increasing. Interestingly, as mentioned earlier, two regular catalyst samples have similar Tafel slopes. From term of theoretical calculation, the adsorption (kinetic) properties of sphere-like is exactly closed to particle-like, and both of them have regular sizes, however the size of Ni(OH)<sub>2</sub>-NPS is actually irregularity, and it owns a significantly lowest Tafel slope. As mentioned above, this subtle difference of Tafel slope clearly illustrates the delicate relationship between the structure and their molecular reactions. The lowest Tafel slope of Ni(OH)<sub>2</sub>-NPS indicates that the particle-sphere-like nanostructure have the most favorable kinetic properties, which promote the process of the OER and enhance the activity.

To compare the intrinsic activities of the above catalysts, the mass activity ( $j_{\text{mass}}$ ) and specific activity ( $j_{\text{BET}}$ ) (the process of calculation is in support information) were calculated at  $\eta = 350$  mV as well (Fig. 3c). From the curves, OER activity could be easily concluded, which is basically matched ignorable.

Electrochemically active surface area (ECSA) is also one of the most representative parameters for OER (Table 1). As is known to all, because of the proportional relationship, the catalyst's electrochemical double-layer capacitance ( $C_{\text{dl}}$ ) reflects ECSA [45, 46].  $C_{\text{dl}}$  was performed by using cyclic

voltammetry (CV) in a non-faradaic region. Specifically, cyclic voltammograms (CVs) in sweeping scan rates ranging from 20 to 200 mV s<sup>-1</sup> were performed with a potential window of 1.01–1.05 V in the non-faradaic region to obtain the capacitive current associated (Figs. 4a and S2). Before testing, 50 cycles of CV between 1.0 and 1.1 V vs. RHE with a scan rate of 500 mV s<sup>-1</sup> were applied to keep the electrode surface stable. Accordingly, the capacitance of Ni(OH)<sub>2</sub>-NPS was estimated by CVs to be 4.1 mF cm<sup>-2</sup>, which was much higher than that of Ni(OH)<sub>2</sub>-NS (0.27 mF cm<sup>-2</sup>) and Ni(OH)<sub>2</sub>-NP (0.09 mF cm<sup>-2</sup>), indicating a larger electrochemically active surface area of the nanoparticle-sphere structure. The results imply that the optimal oxygen evolution reaction electrocatalytic activity of the Ni(OH)<sub>2</sub>-NPS was relevant to the largest ECSA (Fig. 4b) due to the effective electrocatalyst-electrolyte contact interface area. By using the equation:

$$\text{ECSA} = \frac{C_{\text{dl}}}{C_s} \quad (1)$$

$C_s = 0.040$  mF cm<sup>-2</sup> is suitable for specific capacitance [47], the ECSA values of three samples actually differ greatly. The ECSA of Ni(OH)<sub>2</sub>-NPS is 102.5 cm<sup>2</sup>, meanwhile, the ECSA values of Ni(OH)<sub>2</sub>-NS (6.75 cm<sup>2</sup>) are larger than that of Ni(OH)<sub>2</sub>-NP (2.25 cm<sup>2</sup>). Interestingly, Brunauer–Emmett–Teller areas and electrochemical surface areas own slightly different trends, and the BET areas of Ni(OH)<sub>2</sub>-NP are actually larger than that of Ni(OH)<sub>2</sub>-NS, but the ECSA of Ni(OH)<sub>2</sub>-NP is smaller than that of Ni(OH)<sub>2</sub>-NS. Most of their values are mostly within reasonable range and error, which may be due to the difference in testing conditions. That is because the nanoparticle-like powder is more easily exposed to the N<sub>2</sub> atmosphere than nanosphere-like powder. While for the estimation of ECSA, the inevitable particle–particle stacking of the nanoparticle could cause the ECSA to decrease, yet the nanosphere structure can avoid this decrease, due to the nanospheres owing many nanopores which take key roles for the ion to penetrate, so the ECSA value of Ni(OH)<sub>2</sub>-NS is much higher than that of Ni(OH)<sub>2</sub>-NP. Another pivotal kinetic parameter of OER is the turnover frequency (TOF), which reflects the intrinsic characteristics of electrocatalytic activity (Supporting Information).

**Table 1** Comparison of OER activity data calculated from different catalysts

| Catalyst                 | $\eta$ at $j = 10$ mA cm <sup>-2</sup> (mV) | Mass activity at $\eta = 350$ mV (A mg <sup>-1</sup> ) | Specific activity at $\eta = 350$ mV (A m <sup>-2</sup> ) | Tafel slope (mV dec <sup>-1</sup> ) |
|--------------------------|---|--|---|-------------------------------------|
| Ni(OH) <sub>2</sub> -NS  | 450   | 0.025  | 0.015   | 95.4                                |
| Ni(OH) <sub>2</sub> -NP  | 500   | 0.013  | 0.01  | 97.1                                |
| Ni(OH) <sub>2</sub> -NPS | 250   | 0.113  | 0.085   | 74.1                                |
| RuO <sub>2</sub>         | 340   |  |   | 89.2                                |



**Table 2** The summary of OER data from As-synthesized  $\alpha$ -Ni(OH)<sub>2</sub> samples

| Catalyst                 | $\eta$ at $j = 10 \text{ mA cm}^{-2}$ (mV) | $C_{dl}$ (mF cm <sup>-2</sup> ) | ESCA (cm <sup>2</sup> ) | TOF at $\eta = 350 \text{ mV}$ (s <sup>-1</sup> ) |
|--------------------------|--|---------------------------------|-------------------------|---|
| Ni(OH) <sub>2</sub> -NS  | 450  | 0.27                            | 6.75                    | 0.6   |
| Ni(OH) <sub>2</sub> -NP  | 500  | 0.09                            | 2.25                    | 0.1   |
| Ni(OH) <sub>2</sub> -NPS | 250  | 4.1                             | 102.5                   | 38.4  |

According to the results (Table 2), Ni(OH)<sub>2</sub>-NPS catalyst exhibits the highest TOF of 38.4 s<sup>-1</sup> at  $\eta = 350 \text{ mV}$ , while the TOF values of Ni(OH)<sub>2</sub>-NS and Ni(OH)<sub>2</sub>-NP are 0.6 and 0.1 s<sup>-1</sup>, indicating the structures of catalysts affect both kinetics properties and intrinsic activities. From the calculation results based on ECSA, the most irregular-shaped Ni(OH)<sub>2</sub>-NPS keeps the highest TOF value among the three different nanostructure samples, illustrating the specific shape (sphere-particle-like) does increase the intrinsic activity.

In addition, electrochemical impedance spectroscopy (EIS) was performed to support further understanding of the reaction's kinetics of as-prepared catalysts. EIS was measured in the electrolyte of 0.1 M KOH, Ni(OH)<sub>2</sub>-NPS exhibits the smallest semicircle diameter ( $R_{ct} = 52.3 \Omega$ ), (Fig. 4c) which is much smaller than that of Ni(OH)<sub>2</sub>-NP electrode (109.5  $\Omega$ ), Ni(OH)<sub>2</sub>-NS (81.2  $\Omega$ ), and even benchmark catalyst RuO<sub>2</sub> electrode (67.9  $\Omega$ ), suggesting that the high conductivity of Ni(OH)<sub>2</sub>-NPS. Its unique nanostructure causes the synergistic effects, thus nanoparticle-sphere-like Ni(OH)<sub>2</sub> has a prominent advantage over other nanostructures-like Ni(OH)<sub>2</sub> on effective and abundant electrocatalytic active sites due to larger interfaces with the electrolyte and shorter ion diffusion pathways [48, 49]. These results confirm that the nanoparticle-sphere structure can significantly improve the electron transport performance between the electrolyte and electrode, which indeed boost the electrochemical process.

Based on the electrochemical measurements, the prominent advantages of Ni(OH)<sub>2</sub>-NPS, lower overpotential, lower Tafel slope, larger double-layer capacitance and higher intrinsic activity, confirmedly provide that nanoparticle-sphere does boost OER performance and overall water splitting. According to the results obtained, the excellent electrocatalytic properties of the as-prepared sample might be ascribed to the following three points: (i) nanoparticle-sphere structure generate adequate reaction sites, providing more areas to improve catalytic activity (larger  $C_{dl}$ ); (ii) nanoparticle-sphere structure boost much closer contact with the alkaline electrolyte, causing to provide more active sites for ions to react (lower Tafel slope); (iii) nanoparticle-sphere structure is actually open, and gas (O<sub>2</sub>) release and intrinsic activity (higher TOF) are both promoted; (iv) nanoparticle-sphere structure facilitates charge transport (smaller value of  $R_{ct}$ ), reduces resistance and improves catalytic processes. All calculated data of three obtained samples are shown in Table 2. Comparing two

regular samples, Ni(OH)<sub>2</sub>-NS has slightly higher oxygen evolution reaction catalytic activity, mainly because nanosphere structure can provide more areas to improve catalytic activity, and has more reactivity of active sites and owns more open structure to release O<sub>2</sub>. Significantly, the synergistic effect of three advantages does improve catalytic activity, so Ni(OH)<sub>2</sub>-NPS has more areas to improve catalytic activity, more active sites to boost the adsorption capacity of OH<sup>-</sup>, and higher intrinsic activity than Ni(OH)<sub>2</sub>-NS (details in Table 2). As shown in Table 2, for these unique-like samples, the most irregular nanostructure (nanoparticle-sphere) could represent the highest OER activity by simultaneously improving the  $C_{dl}$ , Tafel slope, and TOF compared with sphere-like and particle-sphere-like structures.

Without good stability, an excellent electrocatalyst is out of the question [50, 52, 53]. After 1000 cyclic voltammograms (CVs) electrochemical tests with the sweeping scan rate of 250 mV s<sup>-1</sup> (Fig. 4d), the obtained LSV curve (blue) was close to the first one (red), with the ignorable current density loss and overpotential increase. The long-term durability of the Ni(OH)<sub>2</sub>-NPS was also performed by a chronoamperometry measurement (Fig. 4e) at 1.48 V (vs. RHE,  $j = 10 \text{ mA cm}^{-2}$ ). Clearly, because of the interference of O<sub>2</sub> bubbles generated, the current density fluctuates slightly, and after the 8 h test, it maintains 95% of the current density of 10 mA cm<sup>-2</sup>. This shows that Ni(OH)<sub>2</sub>-NPS has outstanding long-term catalytic stability during oxygen evolution reactions. In fact, by comparing the SEM images before and after the long-term test (Fig. 4e inset), we can find that the Ni(OH)<sub>2</sub>-NPS maintains good morphology and structure. Meanwhile, no significant structural changes are discovered, indicating the excellent structural reliability of this sample. In fact,  $\alpha$ -Ni(OH)<sub>2</sub> is only stable on the electrode surface at low potentials region (below 0.5 V vs. RHE) in alkaline media, afterward converting to the more thermodynamically stable phase of  $\beta$ -Ni(OH)<sub>2</sub>. Additional HRTEM and XPS tests were performed to investigate the chemical composition of the Ni(OH)<sub>2</sub>-NPS after long-term durability testing. From Fig. 5a, the lattice fringe of  $\beta$ -NiOOH is clearly observed, indicating that  $\beta$ -NiOOH is a real active species and plays an important role in the OER reaction. The XPS spectroscopy proves the presence of Ni, O, and Fe elements in the post-experiment Ni(OH)<sub>2</sub>-NPS (Fig. 5b). Because a small amount of Fe is present in KOH, the sample contains

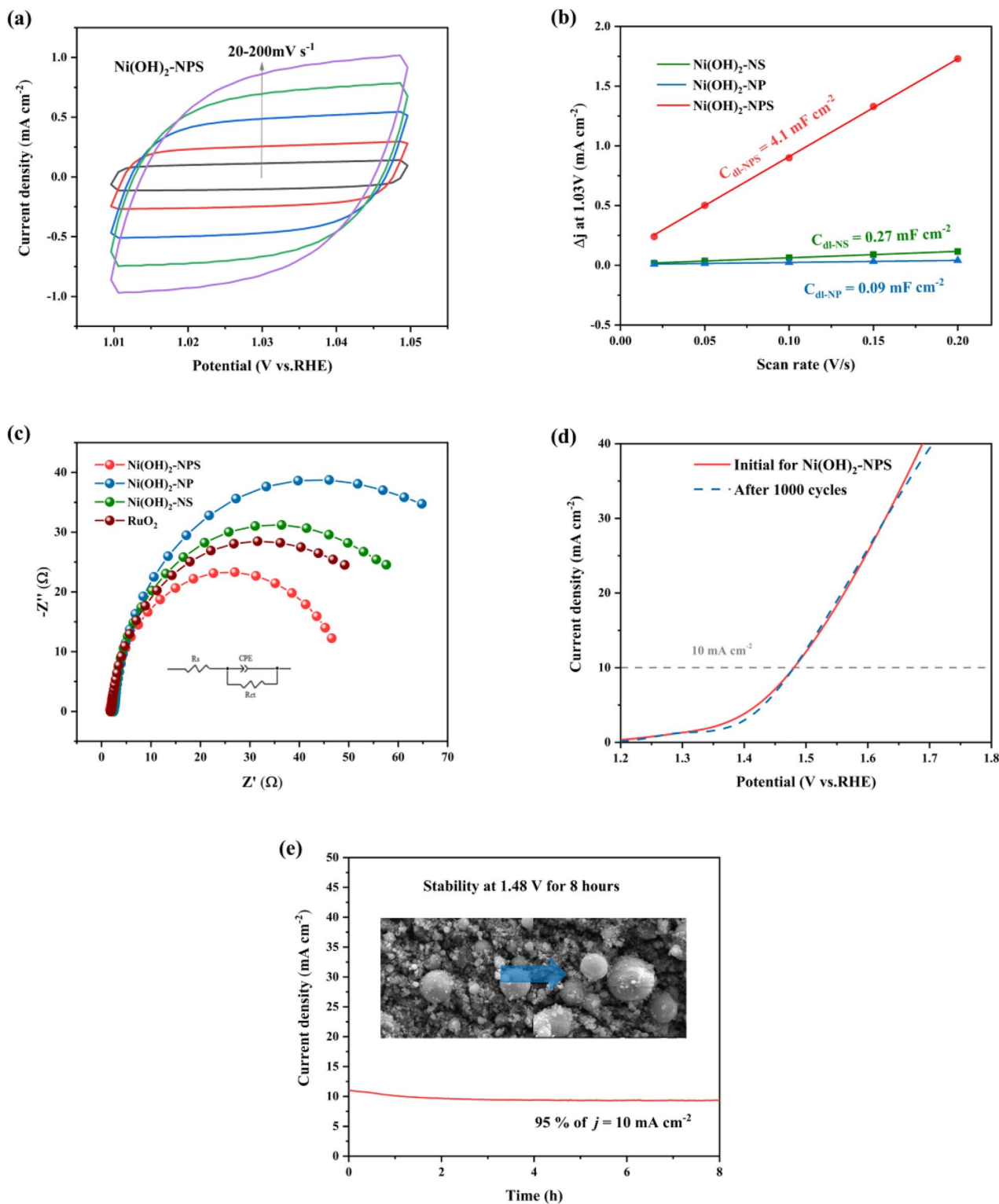


**Fig. 4** **a** Current density measured in non-faradaic potential from 1.01 to 1.05 V at different scan rates, 20, 50, 100, 150, and 200  $\text{mV s}^{-1}$ , for the  $\text{Ni(OH)}_2\text{-NPS}$  sample; **b** the capacitive current as a function of scan rates for different catalysts; **c** EIS for the as-prepared  $\alpha\text{-Ni(OH)}_2$

samples; **d** stability tests of  $\text{Ni(OH)}_2\text{-NPS}$  for 1000 cycles of a CV; **e** chronoamperometry test at 1.48 V ( $10 \text{ mA cm}^{-2}$ ) for 8 h. Insets are the SEM images of  $\text{Ni(OH)}_2\text{-NPS}$  before and after the test.

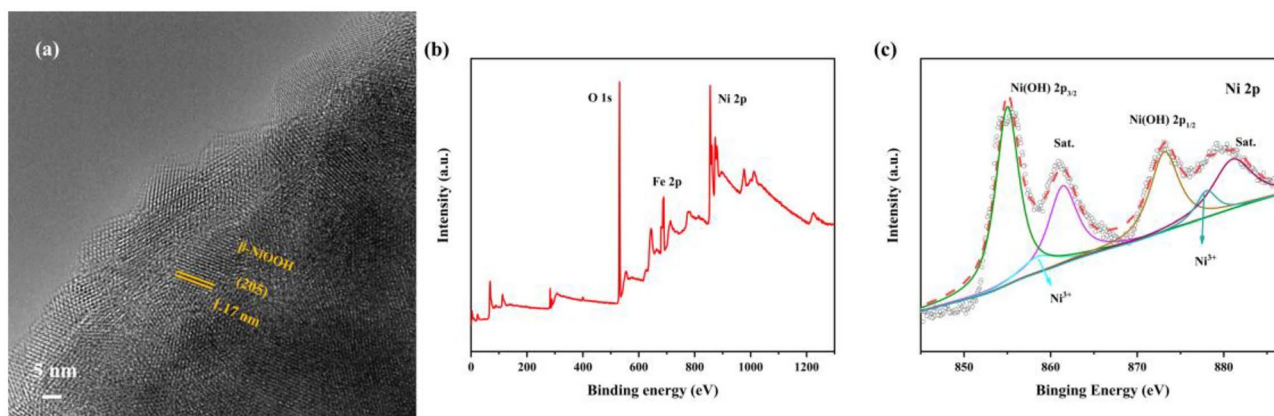


**Fig. 5** **a** HRTEM, **b** XPS, and **c** high-resolution Ni 2p XPS spectra images of post-experiment Ni(OH)<sub>2</sub>-NPS

**Table 3** Summary of literature OER performances of the most typical 2D/3D and polymetal hydroxide catalysts in alkaline electrolytes

| Catalyst   | Electrolyte | $\eta_{j=10}$ (mV) | Tafel slope (mV dec <sup>-1</sup> ) | Reference |
|--|-------------|--------------------|-------------------------------------|-----------|
| NF@NiFe LDH/CeO <sub>x</sub>                       | 1.0 M KOH   | 280                | 101                                 | [50]      |
| P-Co <sub>2</sub> Cr <sub>1</sub> LDHs nanosheets  | 1.0 M KOH   | 285                | 45                                  | [51]      |
| NiMn LDH   | 1.0 M KOH   | 280                | 70                                  | [52]      |
| ZnCo LDH/RGO                                       | 0.1 M KOH   | 430                | 73                                  | [53]      |
| Ni-FeLDH@MnCO <sub>3</sub>                         | 1.0 M KOH   | 275                | 45                                  | [54]      |
| Ni-Co hydroxide nanoplate                          | 1.0 M KOH   | 270                | 59                                  | [55]      |
| Ni-Co LDH/carbon paper                             | 1.0 M KOH   | 367                | 40                                  | [56]      |
| Layered Ni-Co silicate hydroxide nanosheets@MWCNTs | 0.1 M KOH   | 440                | 96                                  | [57]      |
| $\alpha$ -Ni(OH) <sub>2</sub> hollow spheres       | 0.1 M KOH   | 330                | 42                                  | [58]      |
| NiV LDH nanosheet                                  | 1.0 M KOH   | 318                | 50                                  | [59]      |
| $\alpha$ -Ni(OH) <sub>2</sub> -NPS                 | 0.1 M KOH   | 250                | 73.9                                | This work |

a certain amount of Fe (1.2%, Table S2) after the long-time reaction. What is more, the high-resolution XPS spectra of Ni 2p (Fig. 5c) exhibit Ni<sup>3+</sup> signal peaks attributed to the oxidation of Ni<sup>2+</sup> during the long-term durability test. This result is agreed with HRTEM, indicating that  $\beta$ -NiOOH plays an important role in the OER reaction.

In general, Ni(OH)<sub>2</sub>-NPS not only has enough specific surface areas to support active sites but also provides enough ions channels for OH<sup>-</sup> to transfer, meanwhile avoiding the agglomeration of 3D materials through its stable nanostructure. As single metal hydroxide material, nanoparticle-sphere like Ni(OH)<sub>2</sub> reaches the current density of 10 mA cm<sup>-2</sup> only requiring 250 mV overpotential, and maintains excellent performance stability (8 h) after long-term experiment just via design 3D structure. Of note, it is also superior to most polymetal hydroxide OER catalysts, for instance, P-Co<sub>2</sub>Cr<sub>1</sub> LDHs (285 mV) [51], Ni-FeLDH@MnCO<sub>3</sub> (275 mV) [54], and Ni-Co hydroxide nanoplate (270 mV) [55], as well as other two/three-dimensional and polymetal-based OER catalysts, as gathered in Table 3.

## Conclusion

In summary, we successfully synthesized three different 3D nanostructures  $\alpha$ -Ni(OH)<sub>2</sub> samples via a controlling solvothermal system. Three synthesized Ni(OH)<sub>2</sub> samples have different 3D structures, similar BET-specific surface area, and average pore size, which provides a perfect single variable platform for the study of the relationship between their unique structure and OER performance. From the results of systematic experiments and analyses, a more irregular nanoparticle-sphere-like structure (Ni(OH)<sub>2</sub>-NPS) has the best effectively OER catalytic activity, since it owns not only better favorable kinetics properties (Tafel slope), larger accessible surface area ( $C_{dl}$ ), much higher intrinsic activity (TOF) to promote OER performance, but also reliable three-dimensional nanostructures to ensure the durability. Profit by these unmissable characteristics, nanoparticle-sphere-like Ni(OH)<sub>2</sub> has become a promising noble candidate catalyst for OER to popularize, indicating a method of manufacturing improved catalysts from structural design was pointed

out. By comparing three kinds of  $\alpha$ -Ni(OH)<sub>2</sub> samples, the conceptually 3D nanostructures  $\alpha$ -Ni(OH)<sub>2</sub> are presented and demonstrated to be good models for the design of electrocatalysts to optimize OER and water splitting performance. Our study proposes the star effect for the first time and provides a new guiding strategy for the design of effective electrocatalysts for OER by using high-cost performance and easily prepared  $\alpha$ -Ni(OH)<sub>2</sub>.

**Supplementary Information** The online version contains supplementary material available at <https://doi.org/10.1007/s12678-022-00757-z>.

**Acknowledgements** This work was partially sponsored by the National Natural Science Foundation of China (52076126) and the Natural Science Foundation of Shanghai (18ZR1416200). The authors would like to thank Shiyanjia Lab ([www.shiyanjia.com](http://www.shiyanjia.com)) for the support of the SEM, BET, and XPS tests.

## Declarations

**Consent for Publication** This manuscript is original. All authors have approved the submission of the manuscript. This article has not been published and is not being considered for publication elsewhere.

**Conflict of Interest** The authors declare no competing interest.

## References

1. J.K. Hurst, Chemistry. In pursuit of water oxidation catalysts for solar fuel production, *Science* **328**(5976), 315–316 (2010). <https://doi.org/10.1126/science.1187721>
2. K.S. Joya, H.J.M. de Groot, Biomimetic molecular water splitting catalysts for hydrogen generation. *Int. J. Hydrogen Energy* **37**(10), 8787–8799 (2012). <https://doi.org/10.1016/j.ijhydene.2012.01.139>
3. T. Li, X. Ma, J. Wu, F. Chu, L. Qiao, Y. Song, M. Wu, J. Lin, L. Peng, Z. Chen, Ni(OH)<sub>2</sub> microspheres in situ self-grown on ultrathin layered g-C<sub>3</sub>N<sub>4</sub> as a heterojunction electrocatalyst for oxygen evolution reaction. *Electrochimica Acta*. **400**(2021). <https://doi.org/10.1016/j.electacta.2021.139473>
4. T. Li, J. Wu, L. Qiao, Q. Zhu, Z. Fu, J. Lin, J. Chen, L. Peng, B. Wang, Z. Chen, Bimetallic Ni-Hf tellurides as an advanced electrocatalyst for overall water splitting with layered g-C<sub>3</sub>N<sub>4</sub> modification. *Materials Today Energy* **26** (2022). <https://doi.org/10.1016/j.mtener.2022.101002>
5. S. Klaus, Y. Cai, M.W. Louie, L. Trotochaud, A.T. Bell, Effects of Fe electrolyte impurities on Ni(OH)<sub>2</sub>/NiOOH structure and oxygen evolution activity. *J. Phys. Chem. C* **119**(13), 7243–7254 (2015). <https://doi.org/10.1021/acs.jpcc.5b00105>
6. A.G. Oshchepkov, G. Braesch, A. Bonnefont, E.R. Savinova, M. Chatenet, Recent advances in the understanding of nickel-based catalysts for the oxidation of hydrogen-containing fuels in alkaline media. *ACS Catal.* **10**(13), 7043–7068 (2020). <https://doi.org/10.1021/acscatal.0c00101>
7. S. Tahmasebi, S. Jahangiri, N. Mosey, G. Jerkiewicz, A. Mark, S. Cheng, G. Botton, S. Baranton, C. Coutanceau, Remarkably stable nickel hydroxide nanoparticles for miniaturized electrochemical energy storage. *ACS Applied Energy Materials* **3**(8), 7294–7305 (2020). <https://doi.org/10.1021/acsaem.0c00483>
8. Y. Liu, Z. Niu, Y. Lu, L. Zhang, K. Yan, Facile synthesis of CuFe<sub>2</sub>O<sub>4</sub> crystals efficient for water oxidation and H<sub>2</sub>O<sub>2</sub> reduction. *J. Alloy. Compd.* **735**, 654–659 (2018). <https://doi.org/10.1016/j.jallcom.2017.11.181>
9. N. Mirbagheri, J. Chevallier, J. Kibsgaard, F. Besenbacher, E.E. Ferapontova, Electrocatalysis of water oxidation by H<sub>2</sub>O-capped iridium-oxide nanoparticles electrodeposited on spectroscopic graphite. *Chem. Phys. Chem.* **15**(13), 2844–2850 (2014). <https://doi.org/10.1002/cphc.201402079>
10. D. Xiaoqiang, X. Zhoufeng, G. Yaqiong, D. Yong, Polyoxometalate-based catalysts for photocatalytic, chemical catalytic and electrocatalytic water oxidation. *Int. J. Hydrogen Energy* **42**(38), 24169–24175 (2017). <https://doi.org/10.1016/j.ijhydene.2017.08.023>
11. L. Yu, J. Lin, M. Zheng, M. Chen, Y. Ding, Homogeneous electrocatalytic water oxidation at neutral pH by a robust trinuclear copper(ii)-substituted polyoxometalate. *Chem. Commun. (Camb)* **54**(4), 354–357 (2018). <https://doi.org/10.1039/c7cc08301g>
12. K. Zeng, D. Zhang, Recent progress in alkaline water electrolysis for hydrogen production and applications. *Prog. Energy Combust. Sci.* **36**(3), 307–326 (2010). <https://doi.org/10.1016/j.pecs.2009.11.002>
13. H. Dau, C. Limberg, T. Reier, M. Risch, S. Roggan, P. Strasser, The mechanism of water oxidation: from electrolysis via homogeneous to biological catalysis. *ChemCatChem*. **2**(7), 724–761 (2010). <https://doi.org/10.1002/cctc.201000126>
14. E. Mirzakulova, R. Khatmullin, J. Walpita, T. Corrigan, N.M. Vargas-Barbosa, S. Vyas, S. Oottikkal, S.F. Manzer, C.M. Hadad, K.D. Glusac, Electrode-assisted catalytic water oxidation by a flavin derivative. *Nat. Chem.* **4**(10), 794–801 (2012). <https://doi.org/10.1038/nchem.1439>
15. J. Suntivich, K.J. May, H.A. Gasteiger, J.B. Goodenough, Y. Shao-Horn, A perovskite oxide optimized for oxygen evolution catalysis from molecular orbital principles. *Science* **334**(6061), 1383–1385 (2011). <https://doi.org/10.1126/science.1212858>
16. Y. Lee, J. Suntivich, K.J. May, E.E. Perry, Y. Shao-Horn, Synthesis and activities of rutile IrO<sub>2</sub> and RuO<sub>2</sub> nanoparticles for oxygen evolution in acid and alkaline solutions. *J Phys Chem Lett* **3**(3), 399–404 (2012). <https://doi.org/10.1021/jz2016507>
17. J. Luo, J.H. Im, M.T. Mayer, M. Schreier, M.K. Nazeeruddin, N.G. Park, S.D. Tilley, H.J. Fan, M. Gratzel, Water photolysis at 12.3% efficiency via perovskite photovoltaics and earth-abundant catalysts. *Science* **345**(6204), 1593–6 (2014). <https://doi.org/10.1126/science.1258307>
18. J.K. Kim, G.D. Park, J.H. Kim, S.K. Park, Y.C. Kang, Rational design and synthesis of extremely efficient macroporous CoSe<sub>2</sub>-CNT composite microspheres for hydrogen evolution reaction. *Small* **13**(27), (2017). <https://doi.org/10.1002/sml.201700068>
19. T.H. Nguyen, J. Lee, J. Bae, B. Lim, Binary FeCo oxyhydroxide nanosheets as highly efficient bifunctional electrocatalysts for overall water splitting. *Chemistry* **24**(18), 4724–4728 (2018). <https://doi.org/10.1002/chem.201800022>
20. B. Wei, P. Yao, G. Tang, Z. Qi, W. Hu, J. Hong, C. Chen, Z. Wang, Mn-doped CoSe<sub>2</sub> nanosheets as high-efficiency catalysts for the oxygen evolution reaction. *Dalton Trans.* **48**(38), 14238–14241 (2019). <https://doi.org/10.1039/c9dt03108a>
21. X. Xu, F. Song, X. Hu, A nickel iron diselenide-derived efficient oxygen-evolution catalyst. *Nat. Commun.* **7**, 12324 (2016). <https://doi.org/10.1038/ncomms12324>
22. T.N. Lambert, J.A. Vigil, S.E. White, D.J. Davis, S.J. Limmer, P.D. Burton, E.N. Coker, T.E. Beechem, M.T. Brumbach, Electrodeposited Ni(x)Co<sub>(3-x)</sub>O<sub>4</sub> nanostructured films as bifunctional oxygen electrocatalysts. *Chem. Commun. (Camb)* **51**(46), 9511–9514 (2015). <https://doi.org/10.1039/c5cc02262b>
23. Y. Li, M. Zhao, Y. Zhao, L. Song, Z. Zhang, FeNi layered double-hydroxide nanosheets on a 3D carbon network as an efficient electrocatalyst for the oxygen evolution reaction. *Part*

- Part. Syst. Charact. **33**(3), 158–166 (2016). <https://doi.org/10.1002/ppsc.201500228>
24. M. Dinari, H. Allami, M.M. Momeni, A high-performance electrode based on Ce-doped nickel-cobalt layered double hydroxide growth on carbon nanotubes for efficient oxygen evolution. *J. Electroanal. Chem.* **877** (2020). <https://doi.org/10.1016/j.jelechem.2020.114643>
  25. R. Zhang, S. Cheng, N. Li, W. Ke, N, S-codoped graphene loaded Ni-Co bimetal sulfides for enhanced oxygen evolution activity. *Appl. Surf. Sci.* **503** (2020). <https://doi.org/10.1016/j.apsusc.2019.144146>
  26. A. Dutta, S. Mutyala, A.K. Samantara, S. Bera, B.K. Jena, N. Pradhan, Synergistic effect of inactive iron oxide core on active nickel phosphide shell for significant enhancement in oxygen evolution reaction activity. *ACS Energy Lett.* **3**(1), 141–148 (2017). <https://doi.org/10.1021/acsenerylett.7b01141>
  27. J. Masa, I. Sinev, H. Mistry, E. Ventosa, M. de la Mata, J. Arbiol, M. Muhler, B. Roldan Cuenya, W. Schuhmann, Ultrathin high surface area nickel boride (Ni<sub>3</sub>B) nanosheets as highly efficient electrocatalyst for oxygen evolution. *Adv. Energy Mater.* **7**(17), (2017). <https://doi.org/10.1002/aenm.201700381>
  28. B. Li, F. Song, Y. Qian, J. Shaw, Y. Rao, Boron-doped graphene oxide-supported nickel nitride nanoparticles for electrocatalytic oxygen evolution in alkaline electrolytes. *ACS Applied Nano Materials* **3**(10), 9924–9930 (2020). <https://doi.org/10.1021/acsnm.0c01963>
  29. J. Ren, M. Antonietti, T.-P. Feller, Efficient water splitting using a simple Ni/N/C paper electrocatalyst. *Adv. Energy Mater.* **5**(6), (2015). <https://doi.org/10.1002/aenm.201401660>
  30. Z. Pu, Q. Liu, A.M. Asiri, X. Sun, Ni nanoparticles-graphene hybrid film: one-step electrodeposition preparation and application as highly efficient oxygen evolution reaction electrocatalyst. *J. Appl. Electrochem.* **44**(11), 1165–1170 (2014). <https://doi.org/10.1007/s10800-014-0743-6>
  31. X.Q. Shen, K. Xiang, X.-Z. Fu, J.-L. Luo, High active and ultra-stable bifunctional FeNi/CNT electrocatalyst for overall water splitting. *Int. J. Hydrogen Energy* **46**(7), 5398–5402 (2021). <https://doi.org/10.1016/j.ijhydene.2020.11.098>
  32. J. Yu, G. Cheng, W. Luo, Hierarchical NiFeP microflowers directly grown on Ni foam for efficient electrocatalytic oxygen evolution. *J. Mater. Chem. A* **5**(22), 11229–11235 (2017). <https://doi.org/10.1039/c7ta02968c>
  33. J. Du, Z. Zou, A. Yu, C. Xu, Selenization of NiMn-layered double hydroxide with enhanced electrocatalytic activity for oxygen evolution. *Dalton Trans.* **47**(22), 7492–7497 (2018). <https://doi.org/10.1039/c8dt01372a>
  34. Y. Chen, K. Rui, J. Zhu, S.X. Dou, W. Sun, Recent progress on nickel-based oxide(oxy)hydroxide electrocatalysts for the oxygen evolution reaction. *Chemistry* **25**(3), 703–713 (2019). <https://doi.org/10.1002/chem.201802068>
  35. H. Lee, O. Gwon, C. Lim, J. Kim, O. Galindez, G. Kim, Advanced electrochemical properties of PrBa<sub>0.5</sub>Sr<sub>0.5</sub>Co<sub>1.9</sub>Ni<sub>0.1</sub>O<sub>5+δ</sub> as a bifunctional catalyst for rechargeable zinc-air batteries. *ChemElectroChem* **6**(12), 3154–3159 (2019). <https://doi.org/10.1002/celec.201900633>
  36. D. Tang, J. Liu, X. Wu, R. Liu, X. Han, Y. Han, H. Huang, Y. Liu, Z. Kang, Carbon quantum dot/NiFe layered double-hydroxide composite as a highly efficient electrocatalyst for water oxidation. *ACS Appl. Mater. Interfaces* **6**(10), 7918–7925 (2014). <https://doi.org/10.1021/am501256x>
  37. P. Zhao, H. Nie, Z. Zhou, J. Wang, G. Cheng, NiFe-LDH Grown on three-dimensional Cu<sub>3</sub>P nano-array for highly efficient water oxidation. *ChemistrySelect* **3**(28), 8064–8069 (2018). <https://doi.org/10.1002/slct.201801188>
  38. X. Su, Q. Sun, J. Bai, Z. Wang, C. Zhao, Electrodeposition of porous MoO<sub>4</sub><sup>2-</sup> doped NiFe nanosheets for highly efficient electrocatalytic oxygen evolution reactions. *Electrochim. Acta* **260**, 477–482 (2018). <https://doi.org/10.1016/j.electacta.2017.12.110>
  39. L.A. Stern, X. Hu, Enhanced oxygen evolution activity by NiO<sub>x</sub> and Ni(OH)<sub>2</sub> nanoparticles. *Faraday Discuss* **176**, 363–379 (2014). <https://doi.org/10.1039/c4fd00120f>
  40. R. Agoston, M. Abu Sayeed, M.W.M. Jones, M.D. de Jonge, A.P. O'Mullane, Monitoring compositional changes in Ni(OH)<sub>2</sub> electrocatalysts employed in the oxygen evolution reaction. *Analyst* **144**(24), (2019) 7318–7325. <https://doi.org/10.1039/c9an01905g>
  41. S.-Y. Lee, I.-S. Kim, H.-S. Cho, C.-H. Kim, Y.-K. Lee, Resolving potential-dependent degradation of electrodeposited Ni(OH)<sub>2</sub> catalysts in alkaline oxygen evolution reaction (OER): in situ XANES studies. *Appl. Catal. B Environ.* **284** (2021). <https://doi.org/10.1016/j.apcatb.2020.119729>
  42. N. Kim, D. Lim, Y. Choi, S.E. Shim, S.-H. Baeck, Hexagonal β-Ni(OH)<sub>2</sub> nanoplates with oxygen vacancies as efficient catalysts for the oxygen evolution reaction. *Electrochimica Acta.* **324** (2019). <https://doi.org/10.1016/j.electacta.2019.134868>
  43. Z.J. Zhang, Y.J. Zhu, J. Bao, X.R. Lin, H.Z. Zheng, Electrochemical performance of multi-element doped α-nickel hydroxide prepared by supersonic co-precipitation method. *J. Alloy. Compd.* **509**(25), 7034–7037 (2011). <https://doi.org/10.1016/j.jallcom.2011.03.104>
  44. T. Shinagawa, A.T. Garcia-Esparza, K. Takanabe, Insight on Tafel slopes from a microkinetic analysis of aqueous electrocatalysis for energy conversion. *Sci. Rep.* **5**, 13801 (2015). <https://doi.org/10.1038/srep13801>
  45. X. Sun, Q. Shao, Y. Pi, J. Guo, X. Huang, A general approach to synthesise ultrathin NiM (M = Fe Co, Mn) hydroxide nanosheets as high-performance low-cost electrocatalysts for overall water splitting. *J. Mater. Chem. A* **5**(17), 7769–7775 (2017). <https://doi.org/10.1039/c7ta02091k>
  46. J. Yu, G. Cheng, W. Luo, 3D mesoporous rose-like nickel-iron selenide microspheres as advanced electrocatalysts for the oxygen evolution reaction. *Nano Res.* **11**(4), 2149–2158 (2018). <https://doi.org/10.1007/s12274-017-1832-8>
  47. C.C. McCrory, S. Jung, J.C. Peters, T.F. Jaramillo, Benchmarking heterogeneous electrocatalysts for the oxygen evolution reaction. *J. Am. Chem. Soc.* **135**(45), 16977–16987 (2013). <https://doi.org/10.1021/ja407115p>
  48. J. Bao, X. Zhang, B. Fan, J. Zhang, M. Zhou, W. Yang, X. Hu, H. Wang, B. Pan, Y. Xie, Ultrathin spinel-structured nanosheets rich in oxygen deficiencies for enhanced electrocatalytic water oxidation. *Angew. Chem. Int. Ed. Engl.* **54**(25), 7399–7404 (2015). <https://doi.org/10.1002/anie.201502226>
  49. J. Xie, J. Zhang, S. Li, F. Grote, X. Zhang, H. Zhang, R. Wang, Y. Lei, B. Pan, Y. Xie, Correction to controllable disorder engineering in oxygen-incorporated MoS<sub>2</sub> ultrathin nanosheets for efficient hydrogen evolution. *J. Am. Chem. Soc.* **136**(4), 1680–1680 (2014). <https://doi.org/10.1021/ja412963g>
  50. X. Wang, Y. Yang, L. Diao, Y. Tang, F. He, E. Liu, C. He, C. Shi, J. Li, J. Sha, S. Ji, P. Zhang, L. Ma, N. Zhao, CeOx-decorated NiFe-layered double hydroxide for efficient alkaline hydrogen evolution by oxygen vacancy engineering. *ACS Appl. Mater. Interfaces* **10**(41), 35145–35153 (2018). <https://doi.org/10.1021/acsnami.8b11688>
  51. X. Chen, H. Wang, B. Xia, R. Meng, Noncovalent phosphorylation of CoCr layered double hydroxide nanosheets with improved electrocatalytic activity for the oxygen evolution reaction. *Chem. Commun. (Camb)* **55**(80), 12076–12079 (2019). <https://doi.org/10.1039/c9cc06863e>
  52. J. Du, Z. Zou, A. Yu, C. Xu, Selenization of NiMn-layered double hydroxide with enhanced electrocatalytic activity for oxygen evolution. *Dalton Trans.* **47**(22), 7492–7497 (2018). <https://doi.org/10.1039/c8dt01372a>

53. D. Tang, Y. Han, W. Ji, S. Qiao, X. Zhou, R. Liu, X. Han, H. Huang, Y. Liu, Z. Kang, A high-performance reduced graphene oxide/ZnCo layered double hydroxide electrocatalyst for efficient water oxidation. *Dalton Trans.* **43**(40), 15119–15125 (2014). <https://doi.org/10.1039/c4dt01924e>
54. R. Rajendiran, N. Muthuchamy, K.H. Park, O.L. Li, H.J. Kim, K. Prabakar, Self-assembled 3D hierarchical  $\text{MnCO}_3/\text{NiFe}$  layered double hydroxides as a superior electrocatalysts for the oxygen evolution reactions. *J. Colloid. Interface Sci.* **566**, 224–233 (2020). <https://doi.org/10.1016/j.jcis.2020.01.086>
55. Q. Ye, J. Li, X. Liu, X. Xu, F. Wang, B. Li, Surface pattern of NiCo hydroxide nanoplate arrays electrocatalysts for the oxygen evolution reaction. *J. Power Sources* **412**, 10–17 (2019). <https://doi.org/10.1016/j.jpowsour.2018.10.075>
56. H. Liang, F. Meng, M. Caban-Acevedo, L. Li, A. Forticaux, L. Xiu, Z. Wang, S. Jin, Hydrothermal continuous flow synthesis and exfoliation of NiCo layered double hydroxide nanosheets for enhanced oxygen evolution catalysis. *Nano Lett.* **15**(2), 1421–1427 (2015). <https://doi.org/10.1021/nl504872s>
57. C. Qiu, J. Jiang, L. Ai, When layered nickel-cobalt silicate hydroxide nanosheets meet carbon nanotubes: a synergetic coaxial nanocable structure for enhanced electrocatalytic water oxidation. *ACS Appl. Mater. Interfaces* **8**(1), 945–951 (2016). <https://doi.org/10.1021/acsami.5b10634>
58. M. Gao, W. Sheng, Z. Zhuang, Q. Fang, S. Gu, J. Jiang, Y. Yan, Efficient water oxidation using nanostructured alpha-nickel-hydroxide as an electrocatalyst. *J. Am. Chem. Soc.* **136**(19), 7077–7084 (2014). <https://doi.org/10.1021/ja502128j>
59. K. Fan, H. Chen, Y. Ji, H. Huang, P.M. Claesson, Q. Daniel, B. Philippe, H. Rensmo, F. Li, Y. Luo, L. Sun, Nickel-vanadium monolayer double hydroxide for efficient electrochemical water oxidation. *Nat. Commun.* **7**, 11981 (2016). <https://doi.org/10.1038/ncomms11981>

**Publisher's Note** Springer Nature remains neutral with regard to jurisdictional claims in published maps and institutional affiliations.